

Contents lists available at [ScienceDirect](http://www.sciencedirect.com)

Progress in Quantum Electronics

journal homepage: www.elsevier.com/locate/pqe

Review

Nonlinear optics in optical-fiber nanowires and their applications

Fei Xu, Zhen-xing Wu, Yan-qing Lu^{*}

National Laboratory of Solid State Microstructures, College of Engineering and Applied Sciences, Collaborative Innovation Center of Advanced Microstructures, Nanjing University, Nanjing 210093, China

ABSTRACT

We review recent research on nonlinear optical interactions in optical-fiber nanowires (OFNs) with sub-micron transverse dimensions. Such OFNs, which are fabricated from standard optical fibers, offer numerous beneficial optical and mechanical properties, including strong evanescent fields, high flexibility and configurability, a small mass, and low-loss interconnection to other optical fibers and fiberized components. In particular, the strong confinement of light enables a large enhancement of nonlinear interactions and group-velocity dispersion engineering. The combination of these properties makes OFNs ideal for many nonlinear optical applications, including harmonic generation, Brillouin scattering, four-wave mixing, supercontinuum generation, and optomechanics.

With the incorporation of new materials, OFNs should be ideally suited for a host of nonlinear optical interactions and devices and offer great potential in miniature fiber devices for optical telecommunications and optical sensor applications.

1. Introduction

Wagner and Ellis reported the growth of silicon whiskers as early as 1964, and Givargizov et al. elucidated the growth mechanism of Si whiskers in 1975 [1,2]. Extensive investigations were performed into the synthesis, device fabrication, and applications of photonics whiskers, i.e., nanowires, made of a number of materials, for example, metals (gold, silver, etc.), insulators (zinc oxide, aluminum oxide, etc.), semiconductors (silicon, germanium, gallium arsenide, etc.), and polymers. A broad range of techniques, including both top-down and bottom-up approaches, have been developed and applied for the synthesis and fabrication of nanowires, including electron-beam lithography, laser ablation, chemical vapor deposition, and molecular beam epitaxy. However, before 2003, there was little interest in the development of optical-fiber nanowires (OFNs). Notably, Bures and Bilodeau reported their attempts to manufacture sub-wavelength microwires using a top-down process [3,4]. Fiber devices are made of optical fibers with typical diameters of hundreds of micrometers. In 2003, Tong et al. presented a two-step process to fabricate low-loss subwavelength silica wires, and in 2004, Birks, Gilberto, Leon-Saval, Sumetsky, and many other researchers reported producing OFNs with a waist diameter of hundreds of nanometers and a reduced loss using the conventional heat-and-pull tapering technique [5–8]. Subsequently, there were many reports on the fabrication, properties, and applications of OFNs. With the fast development of OFN fabrication technology, numerous novel devices based on OFNs for optical communications, sensing, and lasers have been proposed and demonstrated, for example, resonators, gratings, and couplers. In the future, OFNs may be considered as building blocks for all-fiber circuits.

OFNs with diameters close to the wavelength of propagating light are of interest for a range of emerging fiber-optic linear and nonlinear applications because they offer numerous beneficial optical and mechanical properties, including strong evanescent fields, high flexibility and configurability, low-loss interconnection to other optical fibers and fiberized components, and, in

^{*} Corresponding author.

E-mail address: yqlu@nju.edu.cn (Y.-q. Lu).

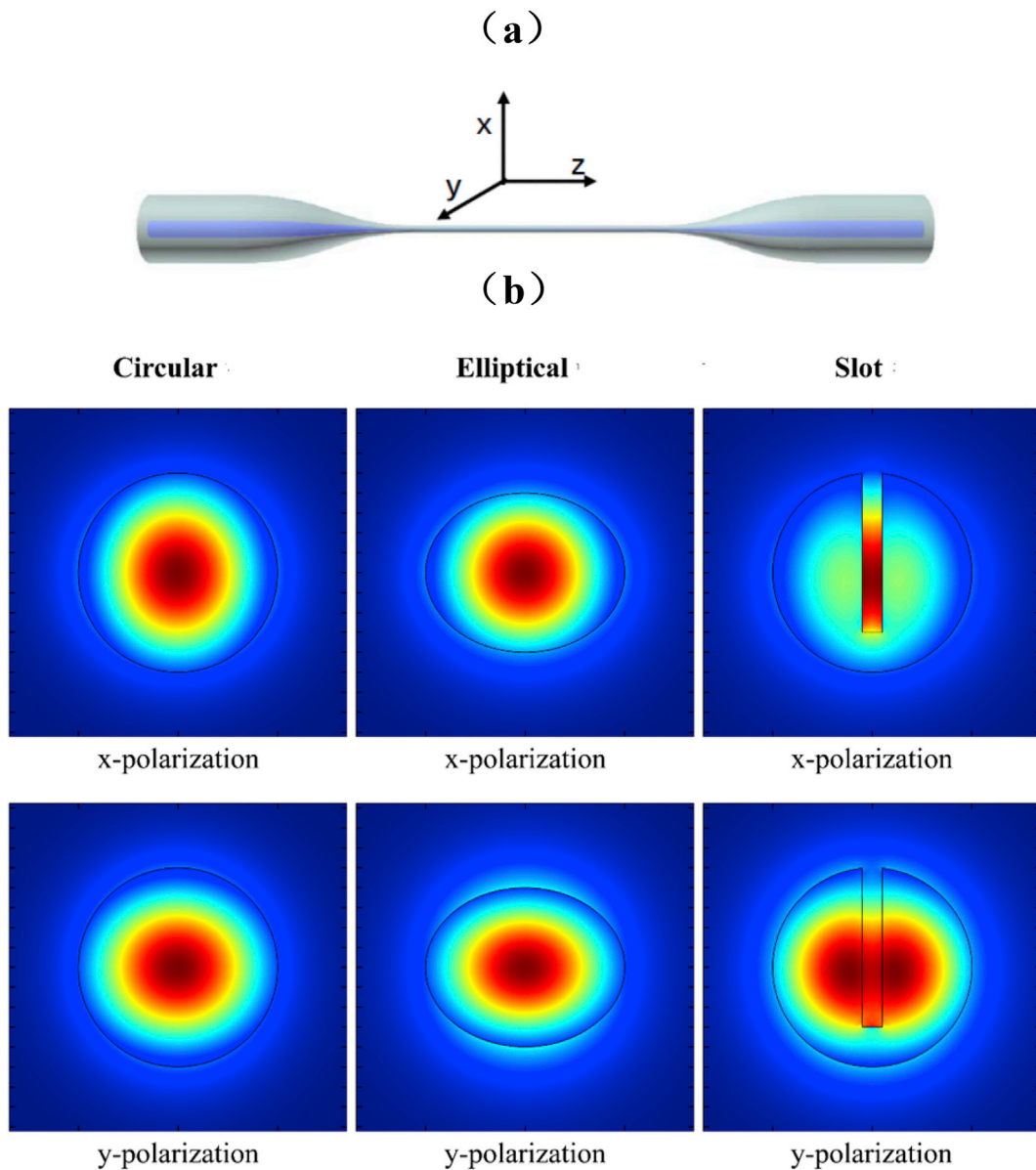


Fig. 1. (a) Structure of an OFN, where z is the propagation direction; (b) the cross sections and power-flow distributions of the fundamental modes with both x-polarization and y-polarization for circular, elliptical, and slot OFNs.

particular, a high nonlinearity. Nonlinear optical processes are useful in all-optical modulators, switches, pulse delays, regenerators, amplifiers, pulse compressors, and wavelength converters. Nonlinear optical processes benefit from large interaction lengths and high optical intensities. The high index contrast of the silica–air waveguide geometry in OFNs allows light to be confined to a very small area over large lengths with a low loss. Additionally, the highly engineerable group-velocity dispersion (GVD), which depends on the OFN diameter, makes it possible to satisfy phase-matching conditions. The combination of these advantages enhances the effective interaction length for nonlinear interactions and allows the ready observation of nonlinear processes, including harmonic generation, Brillouin scattering, four-wave mixing, supercontinuum (SC) generation, and optomechanics. However, the effective interaction length is still limited by the real physical length. So as a pure nonlinear optical conversion device, an OFN could not compete well with regular single-mode fiber (SMF) or photonic crystal fiber (PCF) where the nonlinear interaction length could easily be 100–1000 m, achieving overall high conversions that the OFN could not achieve.

In this study, we review recent research on nonlinear optical interactions in OFNs with the goal of summarizing the wealth of nonlinear effects found in OFNs during the past few years. In the following sections, the linear and nonlinear properties of OFNs are summarized, and the fabrication methodologies are discussed. Thereafter, the various nonlinear effects are reviewed in further detail.

2. Properties of OFNs

2.1. Structure of OFN

An OFN is a fiber taper with a structure comprising a narrow stretched filament (the taper waist), each end of which is linked to upstretched fiber by a conical tapered section (the taper transition), as shown in Fig. 1a. In the past few years, many different methods have been used for fabricating OFNs, and the most popular method is the modified flame-brushing technique. A oxy-butane flame can be used, as well as alternative heat sources such as a carbon-dioxide laser or an electrical microheater. A small heater moves under a stretched optical fiber with two moving translational stages, and the heated area experiences a diameter decrease when stretched. By controlling the relative movement rate of the flame and stages, the fiber is tapered into an OFN with a highly precise shape. The diameter of the fabricated OFN can be as small as tens of nanometers. The technique is not limited to silica fiber: it can also be used to taper a range of glasses, including lead silicate, polymer, silicon, bismuth silicate, and chalcogenide. Generally, the cross section is circular-symmetric, and the OFN has nearly zero birefringence. The characteristics of the OFN, including the dispersion and nonlinearity, mainly depend on one parameter: the diameter. Non-circular-symmetric (NCS) OFNs with more freedom have been proposed and demonstrated by exploiting different structures, including ellipses, slots, the D-shape, and the panda-like shape. Most of these can be fabricated by adiabatically tapering conventional polarization-maintaining fibers, rectangular-shaped fibers, or D-shaped fibers [9–11]. A slot OFN with a low-index slot can be realized by post-processing a circular-symmetric solid OFN [12]. Similar to the slot waveguide in integrated optics [13], a slot OFN can enhance and confine the light field in the nanometer-wide slot. The birefringence can reach 10^{-2} [9–11]. Fig. 1b shows the cross sections and power-flow distributions of the fundamental modes with both x-polarization and y-polarization for circular, elliptical, and slot OFNs. We observe the different mode profiles for the two polarizations in the slot and elliptical OFNs.

2.2. Basic waveguide theory of OFNs

For theoretical design and practical applications of OFNs and OFN devices, it is very important to calculate the propagation constants and/or effective indices, mode characteristics, and dispersion, which requires solving the set of vector Maxwell's equations for the local profile. The waveguide-structure model of the circular OFN without a coating comprises three layers: a core, a cladding, and the environment. When the diameter of the OFN is very small, the core can be ignored, and a two-layer model applies, with the following refractive-index distribution:

$$n = \begin{cases} n_f & \text{in OFN} \\ n_c & \text{out OFN} \end{cases}. \quad (1)$$

In most cases, the OFN is in air; therefore, $n_c = 1$.

We assume that the OFN is non-dissipative and source-free, which is true for most dielectric materials within their transparent ranges. Thus, we can reduce Maxwell's equations to the following equations in cylindrical coordinates (z, ρ, θ):

$$\frac{\partial^2 E_z}{\partial \rho^2} + \frac{1}{\rho} \frac{\partial E_z}{\partial \rho} + \frac{1}{\rho} \frac{\partial^2 E_z}{\partial \theta^2} + [k^2 n^2(\rho, \theta) - \beta^2] E_z = 0, \quad (2)$$

$$\frac{\partial^2 H_z}{\partial \rho^2} + \frac{1}{\rho} \frac{\partial H_z}{\partial \rho} + \frac{1}{\rho} \frac{\partial^2 H_z}{\partial \theta^2} + [k^2 n^2(\rho, \theta) - \beta^2] H_z = 0, \quad (3)$$

where $k = \frac{2\pi}{\lambda}$ is the wave vector, $\beta = 2n_{\text{eff}}k$ is the propagation constant, $n(\rho, \theta)$ is the refractive index, and E_z and H_z are the transverse electrical and magnetic fields, respectively.

The transverse electromagnetic field can be written as follows:

$$\begin{cases} E_\rho = \frac{j}{[k^2 n^2(\rho) - \beta^2]} \left(\beta \frac{\partial E_z}{\partial \rho} + \frac{\omega \mu_0}{\rho} \frac{\partial H_z}{\partial \theta} \right) \\ E_\theta = \frac{j}{[k^2 n^2(\rho) - \beta^2]} \left(\frac{\beta}{\rho} \frac{\partial E_z}{\partial \theta} - \omega \mu_0 \frac{\partial H_z}{\partial \rho} \right) \\ H_\rho = \frac{j}{[k^2 n^2(\rho) - \beta^2]} \left(\beta \frac{\partial H_z}{\partial \rho} + \frac{\omega \epsilon_0 n^2(\rho)}{\rho} \frac{\partial E_z}{\partial \theta} \right) \\ H_\theta = \frac{j}{[k^2 n^2(\rho) - \beta^2]} \left(\frac{\beta}{\rho} \frac{\partial H_z}{\partial \theta} + \omega \epsilon_0 n^2(\rho) \frac{\partial E_z}{\partial \rho} \right) \end{cases}, \quad (4)$$

where ϵ_0 and μ_0 are the electric permittivity and magnetic permeability, respectively, of vacuum.

The propagation constants (β) of air-cladding OFNs are obtained numerically using these equations. However, we only can use the finite-element method or the finite-difference time-domain method to numerically model NCS OFNs such as slot OFNs. To obtain the

index of fused silica, the Sellmeier-type dispersion formula (at room temperature) is applied [14]:

$$n_{\text{silica}}(\lambda) = \sqrt{1 + c_1\lambda^2/(\lambda^2 - c_4) + c_2\lambda^2/(\lambda^2 - c_5) + c_3\lambda^2/(\lambda^2 - c_6)}. \quad (5)$$

The wavelength λ is in μm , and $c_1 = 0.6965325$, $c_2 = 0.4083099$, $c_3 = 0.8968766$, $c_4 = 4.368309 \times 10^{-3}$, $c_5 = 1.394999 \times 10^{-2}$, and $c_6 = 9.793399 \times 10^1$.

Fig. 2 shows the diameter-dependent effective index of silica OFNs at the wavelength of 1550 nm, where the wire diameter (d) is directly related to the V-number: $V = k_0 d (n_f^2 - n_c^2)^{0.5} / 2$. Clearly, when the OFN diameter is reduced to a certain value (corresponding to $V = 2.405$), only the HE_{11} mode exists, corresponding to single-mode operation.

In practical applications related to sensing and nonlinear effects, it is very important to know the power distribution in waveguides. The time-averaged Poynting-vector component along the z-axis per unit area is expressed as [15].

$$S_z = \frac{1}{2} \left(\vec{E} \times \vec{H}^* \right) \cdot \vec{u}_z = \frac{1}{2} (E_r H_\theta^* - E_\theta H_r^*), \quad (6)$$

where \vec{u}_z is a unit vector in the z-direction, and \vec{E} and \vec{H} represent the spatial distributions of the electric and magnetic fields, respectively.

The power fraction carried by the optical core for the two-layer model can be defined as

$$\tau = \frac{\int_0^{2\pi} \int_0^{d/2} S_z dA}{\int_0^{2\pi} \int_0^{d/2} S_z dA + \int_0^{2\pi} \int_{d/2}^{\infty} S_z dA}, \quad (7)$$

where $dA = \rho d\rho d\theta$.

Fig. 3 shows the fractional power as a function of the diameter d . Less than 5% of the power is in the core when the diameter is smaller than 0.4 μm , and more than 90% is in the core when the diameter is larger than 1.5 μm .

2.3. Optical nonlinearity

Optical nonlinearity can significantly degrade the information capacity and limit the channel power in high-speed and long-range optical communications. Nonlinear fiber optics has been widely investigated in standard fiber systems and introduced in the classic textbook [16]. However, OFNs exhibit strong nonlinearity because light can be confined to a very small nonlinear region, allowing the ready observation of nonlinear interactions at relatively low power levels.

When 1 W of optical power propagates in a 10- μm -core SMF, the optical power density is higher than 1 MW/cm^2 and increases by a factor of more than 100 in a 1- μm -diameter OFN. Such a high power density results in the feature of optical nonlinearity in OFNs.

At such a high intensity, the refractive index of silica behaves nonlinearly and increases with the intensity, although it is assumed to be power-independent at low intensities. This is the optical Kerr effect. The physical origin of this effect is the nonlinear susceptibility arising from the harmonic response of electrons to optical fields [17].

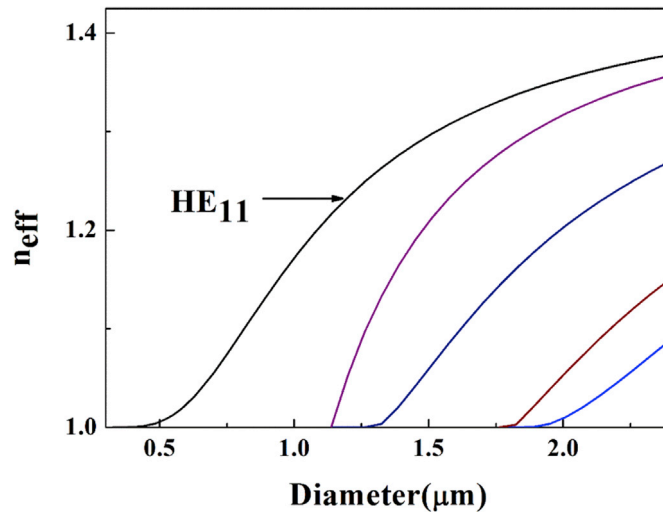


Fig. 2. Effective-index values for the fundamental and high-order modes propagating in an air-cladding OFN as a function of the diameter, calculated according to the exact solution of the Maxwell's equations.

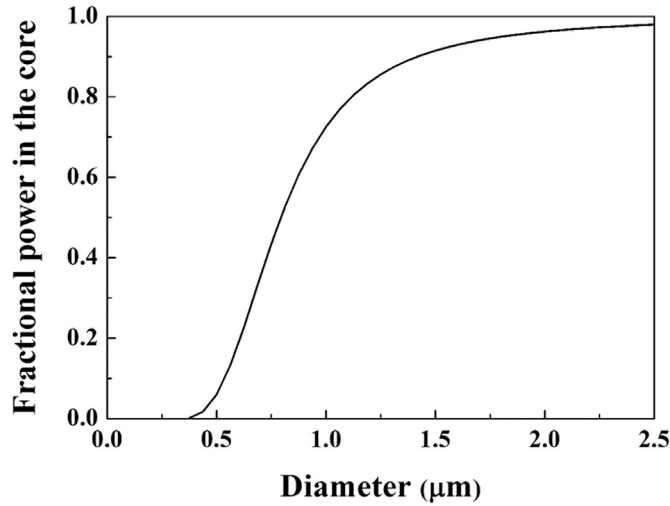


Fig. 3. Fractional power in the core as a function of the diameter.

The nonlinear refractive index is expressed as $n_2 E^2$, where n_2 is the Kerr coefficient related to the third-order susceptibility $\chi^{(3)}$. It is typically given by $n_2 = 2.6 \times 10^{-20} \text{ m}^2/\text{W}$ for silica [18] and $n_2 = 5.0 \times 10^{-23} \text{ m}^2/\text{W}$ for air [17]. The Kerr effect leads to self- and cross-phase modulations (SPM, XPM) of the propagating signal, and other nonlinear phenomena can be produced by utilizing the Kerr effect, for example, optical solitons, optical pulse compression, and modulational instabilities.

The nonlinear coefficient is defined as [14].

$$\gamma = \frac{n_2 \omega}{c A_{eff}} \tag{8}$$

where c is the speed of light in air, ω is the angular frequency, and A_{eff} is the effective area, which is defined as

$$A_{eff} = \frac{\left\{ \int_0^{2\pi} \int_0^\infty |\vec{E}(r, \theta)|^2 r dr d\theta \right\}^2}{\int_0^{2\pi} \int_0^\infty |\vec{E}(r, \theta)|^4 r dr d\theta}, \tag{9}$$

However, the nonlinear coefficient (γ) of the waveguide with a non-circular cross section must be determined as [18].

$$\gamma = k \left(\frac{\epsilon_0}{\mu_0} \right) \frac{\int n^2(x, y) n_2(x, y) \left[2|\vec{E}|^4 + |\vec{E}^2|^2 \right] dA}{3 \left| \int (\vec{E} \times \vec{H}^*) \cdot \hat{z} dA \right|^2}, \tag{10}$$

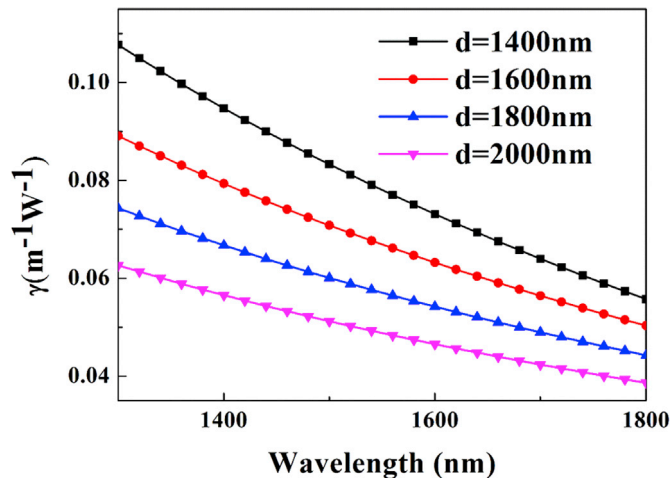


Fig. 4. Nonlinear-coefficient profiles of circular OFNs with different diameters [19].

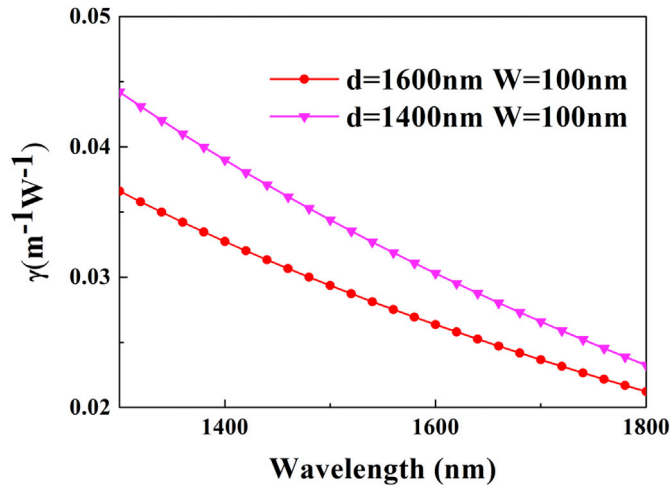


Fig. 5. Nonlinear-coefficient profiles of slot OFNs with different diameters and a width of 100 nm [19].

where n and n_2 are the spatial distribution of the refractive index and the nonlinear-index coefficient, and \hat{z} is the unit vector in the propagation direction.

Fig. 4 depicts the nonlinear coefficient of a circular OFN with different diameters with respect to the wavelength. Clearly, with a smaller diameter, a larger nonlinear coefficient can be obtained because the field intensity of the fiber increases as the diameter decreases.

For comparison, we plotted the nonlinear-coefficient profiles for a slot OFN, as shown in Fig. 5. The plot shows that the nonlinear coefficient increases with the fiber diameter, which is because more light is confined in the low nonlinear-index coefficient air-slot region, and this part of light contributes little to the nonlinear coefficient. The nonlinear coefficient can decrease to $\sim 40\%$ for a slot OFN compared with a circular CMF of the same diameter [19].

The optical Kerr effect is enhanced in OFNs and in principle can be used to induce a nonlinear phase shift via SPM or XPM for diverse nonlinear applications. However, a high-power laser pulse is required because of the limited OFN length. Thus, many researchers have investigated the optical nonlinearity in OFN resonators, which can equivalently increase the interaction length, allowing the bistable behavior to be predicted [20]. A nonlinear optical phase shift can also be realized via thermal effects [21], but the associated time constant is on the order of 1 ms [22], and thermal effects should average out when short optical pulses are used in the resonator. With pico- or nanosecond pulses, which are typical in telecommunications, nonlinear operation can rely on the quasi-instantaneous optical Kerr effect [22]. Coillet et al. compared and analyzed the slow thermal and fast Kerr nonlinearity [22].

2.4. Dispersion

The GVD, i.e., chromatic dispersion, is a primary cause of concern in dealing with short-duration pulses for high-bitrate single-mode wavelength-division multiplexing (WDM) systems because light from a typical optical source contains different wavelength components that travel at different speeds. Furthermore, pulses broaden because of dispersion. There are two main results for material dispersion and waveguide dispersion, and GVD is a very important parameter in all fiber nonlinear applications.

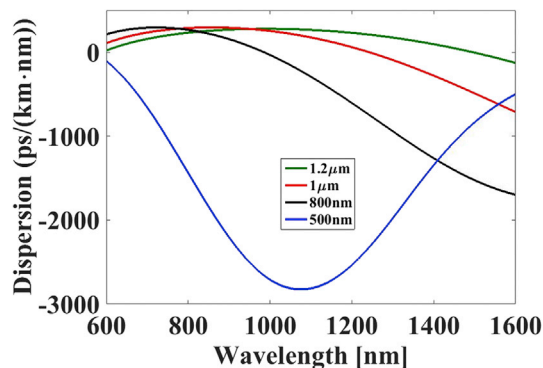


Fig. 6. Dependence of the GVD on the wavelength for four different OFN diameters.

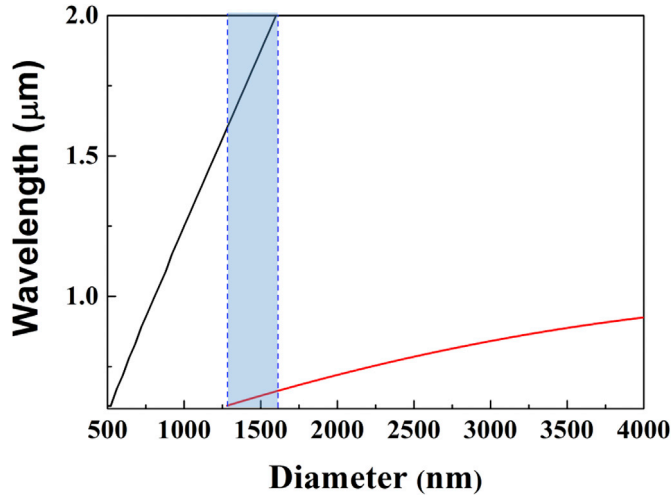


Fig. 7. Zero-GVD wavelength of OFNs in the range of 0.6–2 μm as a function of the diameter. There are two zero-dispersion wavelengths in the blue area (1280–1600 nm). (For interpretation of the references to colour in this figure legend, the reader is referred to the web version of this article.)

The dispersion curve (as a function of the optical frequency) is commonly expanded as a Taylor series with dispersion coefficients β_n . The Taylor coefficient β_2 (ps^2/km) is related to the engineering unit for the GVD— D ($\text{ps}/(\text{nm}\cdot\text{km})$)—as follows [14]:

$$D = -\frac{2\pi c}{\lambda^2} \frac{d^2\beta}{d\omega^2} \quad (11)$$

Fig. 6 shows the dependence of the OFN GVD on the wavelength for five different diameters. The GVD values are large in the normal-dispersion regime: on the order of thousands of $\text{ps}/(\text{nm}\cdot\text{km})$. There are two zero-dispersion points in the d range of 1280–1600 nm, as shown in Fig. 7. The large difference between the refractive indices of the fiber material and air limits the position and the extent of spectral broadening.

However, in some applications, it is difficult to achieve dispersion flattening, even in air-cladding sub-wavelength OFNs. It is possible to realize an ultra-flattened low dispersion over a wide wavelength range in a slot OFN because of the greater structural freedom.

Fig. 8 shows dispersion profiles optimized by tuning these parameters, with a low dispersion of ± 10 $\text{ps}/(\text{nm}\cdot\text{km})$ over a bandwidth in excess of 300 nm at wavelengths ranging from 1300 to 1700 nm.

Additionally, there is significant coupling dispersion in OFN devices based on evanescent-field coupling, such as microcoil resonators, which have a coupling region that consists of adjunct OFNs. Because of the large coupling strength and long coupling length among two or more adjunct OFNs, the coupling dispersion becomes increasingly significant. Thus, we must consider both waveguide and coupling contributions to the dispersion characteristics of OFN microcoil resonators. Simulation results show that the large coupling strength and dispersion have notable contributions to the total microcoil resonator dispersion [23]. When the OFN diameter is in 1.5–5 μm , the total dispersion can be well suppressed because the waveguide dispersion and coupling dispersion almost cancel each other, which is desired in high-speed (10 Gb/s and beyond) optical systems. On the other hand, both positive and negative dispersion can be obtained by adjusting the OFN- microcoil-resonator parameters [23].

3. Parametric processes

3.1. Third-harmonic generation (THG)

The generation of harmonics is a convenient method for producing new short wavelengths. THG is a common process of nonlinear optical frequency conversion from an infrared source to an ultraviolet source in optical fibers and has numerous applications ranging from signal processing to material processing. However, in recent years, THG in OFNs has attracted considerable attention because of their compact size, enhanced nonlinearity, and flexible dispersion. Thus, all-fiber THG systems have potential as a more robust alternative to the existing nonlinear-crystal technologies.

In THG, three fundamental-wave photons interact with nonlinear materials and produce a new photon. Because the wavelength of this photon is one-third of that of the fundamental wave, its frequency is triple that of the fundamental wave. Throughout the whole THG process, the photon satisfies the conservation of momentum and energy, as shown in Fig. 9, where ω_1 and ω_3 are the angular frequencies of the fundamental wave and THG, respectively.

THG is described by the following coupled-mode equations:

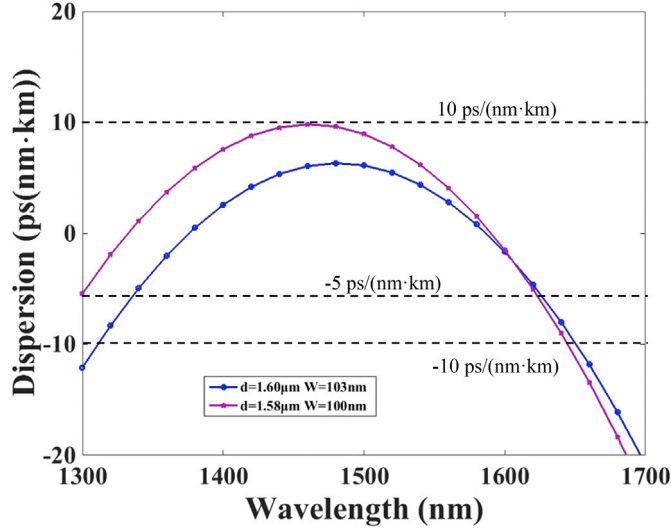


Fig. 8. Optimized dispersion profiles of a slot OFN with flattened near-zero dispersion. One has low dispersion of ± 10 ps/(nm·km) over bandwidth in excess of 340 nm from a wavelength of 1320 nm–1660 nm. Another one has low dispersion value of -5 to 10 ps/(nm·km) over a 340 nm wavelength range, from 1300 nm to 1640 nm.

$$\frac{\partial A_1}{\partial z} = in_2k_1 [(J_1|A_1|^2 + 2J_2|A_3|^2)A_1 + J_3A_1^*A_3e^{i\Delta\beta z}] \tag{12}$$

$$\frac{\partial A_3}{\partial z} = in_2k_1 [(6J_2|A_1|^2 + 3J_5|A_3|^2)A_3 + J_3^*A_1^3e^{i\Delta\beta z}] \tag{13}$$

where A_1 and A_3 are the amplitudes of the fundamental and third-harmonic mode, respectively. $A_j = \vec{E}_j / \left(\frac{\vec{F}_j}{2} \sqrt{\frac{\mu_0}{\epsilon_0}} \right)$ and A_j ($j = 1, 3$) are directly related to their powers, i.e., $A_j(z)^2 = P_j(z)$, which means that the units of A_j are $W^{1/2}$. F_j ($j = 1, 3$) is the transverse electric field. J_1, J_2 and J_5 are the overlap integrals of pump SPM, XPM and harmonic SPM, respectively. For efficient THG, J_3 -the pump-harmonic mode overlap-must be large enough. It can be calculated as $J_3 = \iint_{A_{NL}} (\vec{F}_1 \cdot \vec{F}_3) (\vec{F}_1^* \cdot \vec{F}_1) dS$. When 1064-nm light is pumped into an OFN with a diameter of 520 nm, $J_3 = 0.70 \mu m^{-2}$ [24].

We know that the efficiency $\propto \left(\int_0^L e^{-i\Delta\beta z} dz \right)^2$. Thus, efficient THG requires the satisfaction of the phase-matching condition $\Delta\beta = \beta_3 - 3\beta_1 = 0$, where β_1 and β_3 are the propagation constants of the fundamental wave and THG, respectively.

As with other nonlinear harmonic conversion processes, phase matching should attain efficient THG in OFNs. However, because of the material and waveguide dispersions, only intermodal phase matching can be achieved directly in silica OFNs. In OFNs, the phase-matching condition can be achieved if the modal dispersion compensates for the material dispersion. Thus, we should make the fundamental mode of the fundamental wave equal to higher-order mode of the third harmonic at a certain wavelength. Fig. 10 shows the calculated effective index for both the 1064-nm fundamental wave and 533-nm THG. Intermodal phase matching can be achieved at the cross-points. However, because of the poor mode overlapping, only THG at HE_{12} is easily excited.

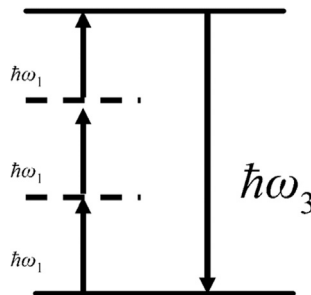


Fig. 9. Process of THG.

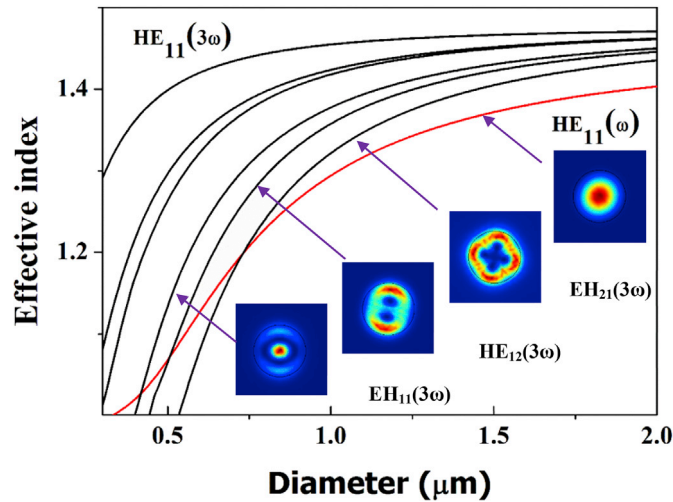


Fig. 10. Phase matching of THG. The red line shows the fundamental mode of the fundamental wave at 1064 nm, and the blue lines show the third harmonic at 355 nm. (For interpretation of the references to colour in this figure legend, the reader is referred to the web version of this article.)

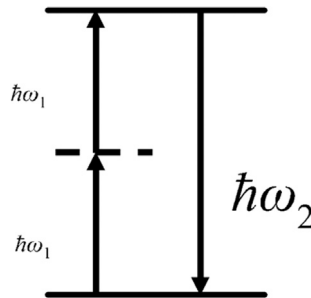


Fig. 11. Process of SHG.

In 1993, an experiment showed that the germanium doping concentration can affect THG [25]. In 2000, THG first was observed in an OFN when 1-kW pulse light was pumped into the OFN, which was 50 cm long [26]. In 2005, Victor Grubsky and Arthur Savchenko introduced a rigorous theory of THG in OFNs [24], and then the third-harmonic wavelength was extended to visible light and ultraviolet [27,28]. The nonlinear interaction length is limited by the fabrication technique for OFN drawing. Ismael et al. used a loop resonator to enhance THG, with up to 7.7 dB gain for the same pump parameters [29].

Nonuniform taper transition regions (rather than the waist) can also be used to generate third harmonics. The range of diameters in taper transition permits phase matching over a large bandwidth. In 2012, Lee et al. fabricated an OFN up to 4.5 cm long with a waist diameter below 2.5 μm to allow a 1.55- μm pump to phase-match with several higher-order third-harmonic modes. When 4-ns pulses with a peak power of 1.25 kW were pumped into OFNs, the conversion rates were up to 3×10^{-4} [30]. Analysis of the third-harmonic frequencies generated from the nonlinearly broadened pump components indicate a 5-dB conversion bandwidth of at least 36 nm, with harmonic power detected over a 150-nm range [30].

3.2. Surface second-harmonic generation (SHG)

Because of the macroscopic central symmetry of the silica, the $\chi^{(2)}$ and the second harmonic (SH) cannot be generated in fibers. However, when a pump pulse with high power is launched into fiber, the SH is generated accidentally [31,32]. In 1986, Österberg et al. reported SHG with a peak power conversion efficiency as high as $\sim 3\%$ in optical fibers [33]. A subsequent study revealed that the SHG is caused by the formation of a second-order susceptibility ($\chi^{(2)}$) grating through multiphoton processes involving both pump and SHG light [34]. However, it has been proven impossible to improve the SHG conversion efficiency beyond a few percent because of the self-saturation effect caused by the interference of the SHG light with the $\chi^{(2)}$ grating [34].

In an OFN, a submicrometric diameter calls for reexamination of interface and bulk multipole moment contributions to $\chi^{(2)}$ [35]. OFNs can provide a higher surface nonlinearity of the core-cladding interface and the nonlinearity of the bulk multipole, which becomes the major mechanism for SHG. Furthermore, a large core-cladding index contrast makes it possible to achieve SHG phase matching in a low-order mode with a sufficient surface intensity [35]. SHG was observed as an unexpected byproduct by

Grubsky et al. in a ~ 500 -nm OFN when they measured THG, and they attributed it to the surface nonlinearity of the OFN [28]. In 2010, Lagsgaard introduced a rigorous theory of surface SHG in OFNs [36]. However, surface SHG is very weak; thus, Gouveia et al. enhanced it using an OFN loop resonator [37]. In Gouveia's experiment, an efficiency up to 4.2×10^{-8} was achieved via pumping with 5-ns 1.55- μm pulses with a peak power of 90 W, and the efficiency was resonantly enhanced by a factor of 5.7 after the OFN was reconfigured as a 1-mm-diameter loop [37]. Recently, another experiment based on an OFN with a periodic nonlinear coating was performed, revealing that the quasi-phase-matched SHG is 15 times stronger than that for the same OFN with a uniform nonlinear coating [38].

Similar to THG, SHG involves two fundamental-wave photons interacting with a nonlinear material and producing a new photon, as shown in Fig. 11.

For an OFN, the coupled-mode equation in the small-signal limit is as follows:

$$\frac{\partial A_2}{\partial z} - i\rho_2 A_1^2 \exp(i\Delta\beta z) = 0.$$

Here, A_1 and A_2 are the field amplitudes of the fundamental and SHG waves, respectively, $\Delta\beta = 2\beta_1 - \beta_2$ is the phase mismatch, and ρ_2 is the overlap integral [5], which is defined as follows:

$$\rho_2 = \frac{\omega_2}{4N_1\sqrt{N_2}} \int \frac{\overrightarrow{2E_2^*}}{\int (\overrightarrow{E_2^*} \times \overrightarrow{H_2}) \cdot \overrightarrow{z} dl} \cdot \overrightarrow{\mathbf{P}}^{(2)} dl. \quad (14)$$

Here, ω_2 is the angular frequency of the SHG wave, and all the field components are normalized by the normalizing factors N_1 and N_2 . The function is integrated over the cross-sectional region of the fiber, and dl is the area element.

Surface contribution is the major mechanism for SHG in nanofibers; thus, the second-order nonlinear polarization $\overrightarrow{\mathbf{P}}^{(2)}$ can be divided into three distinct surface nonlinear-polarization terms, which can be experimentally measured [36,39].

The intermodal phase matching is similar to that of THG. For perfect phase matching, the conversion efficiency can be given as

$$\eta = (\rho_2 z)^2 P_1. \quad (15)$$

In Eq. (15), we observe that the SHG power-conversion efficiency scales linearly with $(\rho_2)^2$ when the pump power P_1 and the interaction length z are fixed. Thus, we compare the SHG conversion capability of different OFNs according to the absolute value of ρ_2 . For silica OFNs, an alternative way to increase ρ_2 is to apply a high intensity to a larger surface. In a slot OFN, an extra nano-slot light field can be enhanced and confined in the sub-wavelength air slot, providing a higher light intensity than the external surface of the circular OFN. Thus, it is possible to have stronger SHG in slot OFNs. Fig. 12 compares the calculated ρ_2 of circular OFNs and slot OFNs, indicating that the ρ_2 of slot OFNs can be as high as five times that in circular OFNs, which equals an SHG conversion efficiency of ~ 25 times that in circular OFNs [35]. In the simulation for a circular OFN, pump light is assumed to propagate in the HE_{11} mode, whereas SHG light is assumed to be generated in the HE_{21} mode of the same polarization. For a slot OFN, the pump and SHG signals are assumed to propagate in the y -polarization of the fundamental mode and the HE_{21} -like mode (the 5th mode), respectively [35].

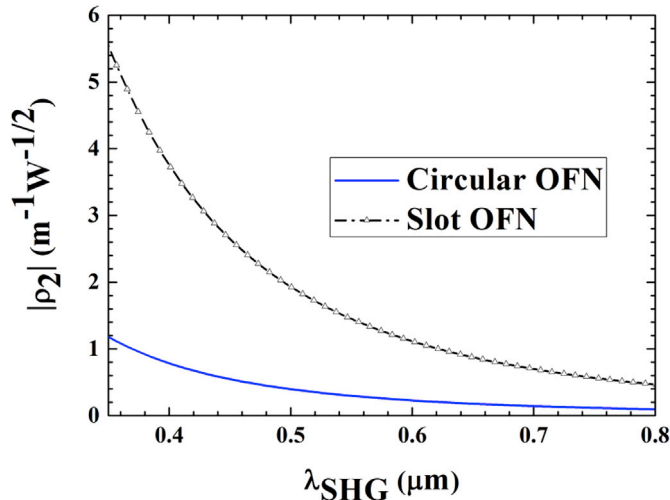


Fig. 12. Relationship between $|\rho_2|$ and the SHG wavelength (λ_{SHG}) for circular OFNs and slot OFNs.

3.3. Four-wave mixing (FWM)

FWM in fibers originates from the nonlinear responses to the light field of the bound electrons. Two pump lights with a high power (P_1 and P_2) in the launched fiber, with the condition of phase matching, result in a higher frequency of Stokes light and a lower frequency of anti-Stokes light. The whole process involves the annihilation of two pump photons (ω_{p1} and ω_{p2}) and the subsequent production of two new photons, whose frequencies are ω_s (signal) and ω_i (ideal). Because of the conservation of momentum and energy, $\omega_{p1} + \omega_{p2} = \omega_s + \omega_i$, as shown in Fig. 13.

There are two important concepts of FWM—parametric gain (g) and effective phase mismatch (δ):

$$\begin{cases} \delta = \Delta k + \gamma(P_1 + P_2) \\ g = \sqrt{(\gamma P_0 \xi)^2 - \left(\frac{\delta}{2}\right)^2}, \end{cases} \quad (16)$$

where $P_0 = P_1 + P_2$, $\xi = \frac{2\sqrt{P_1 P_2}}{P_0}$, and $\Delta k = \beta_{p1} + \beta_{p2} - \beta_s - \beta_i$.

The overlap integral of FWM can be calculated using the following equation [40]:

$$f = \frac{\langle \vec{E}_{p1}^* \vec{E}_{p2}^* \vec{E}_i^* \vec{E}_s^* \rangle}{\left[\langle |\vec{E}_{p1}|^2 \rangle \langle |\vec{E}_{p2}|^2 \rangle \langle |\vec{E}_i|^2 \rangle \langle |\vec{E}_s|^2 \rangle \right]^{\frac{1}{2}}} \quad (17)$$

The phase matching depends on the pump power because of SPM and XPM. If all the frequencies are similar, Δk is relatively small. It is relatively easy to satisfy $\delta = 0$ in the specific case of degenerate FWM with $\omega_{p1} = \omega_{p2}$. This partially degenerate case is most relevant for optical fibers.

Fig. 14 shows the phase mismatching of a 1.7- μm -diameter OFN in air, water, and methanol. The pump wave has a wavelength of 1064 nm. The phase-matched Stokes and anti-Stokes waves are observed at the cross-points along the line of $\delta = 0$. The phase-matched Stokes and anti-Stokes waves can shift considerably with different phase-matched materials.

These results show that FWM is sensitive to the environment, which suggests the feasibility of using FWM as the sensing principle for fiber-optic strain, temperature, or refractive-index sensors. The strain-induced wavelength shift of FWM Stokes waves has been numerically demonstrated. At a pump wavelength of 1550 nm, a strain sensitivity of 2.46 p.m./ $\mu\epsilon$ was obtained, the peak power was 100 W, and the wavelength-shift range was more than 74 nm within a reasonable strain range [41].

Experimental work on FWM in thin OFNs was uncommon until several years ago. In 2002, nondegenerate FWM was investigated and realized in an 18-cm-long tapered microstructure fiber [42]. Later, Turke et al. reported stimulated cascaded FWM in a 2.55- μm OFN (zero-dispersion wavelength ~ 785 nm) by synchronizing a pump pulse that was very close to the zero-dispersion point of the fiber with an additional signal pulse [43]. In 2012, Li et al. utilized two synchronized picosecond lasers (850 nm) to generate octave-spanning cascaded FWM spanning from a few hundred nanometers to almost one octave [44]. In 2013, correlated photon pairs were generated in a 15-cm-long OFN by spontaneous FWM [45]. In 2016, by changing the diameter of the OFN, researchers from the University of Southampton realized parametric amplification of more than 25 dB from the initial signal via FWM in a 6-mm-long OFN [46].

Finally, some external materials can also be induced to modify the OFN characteristics and generate FWM. Wu et al. used a graphene-coated OFN to perform multi-order cascaded FWM [47].

4. Stimulated Brillouin scattering (SBS)

SBS in optical fibers is a fundamental third-order nonlinear process between optical waves and acoustic waves and has been widely investigated and applied for signal processing and sensing. Recently, new findings in nanoscale silicon waveguides have revealed that

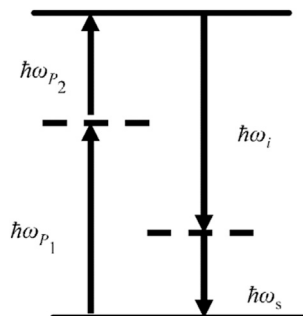


Fig. 13. Process of FWM.

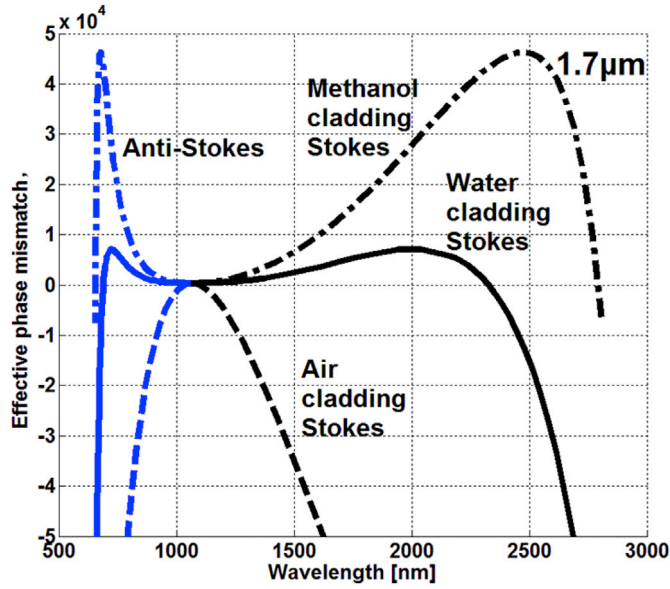


Fig. 14. Relationship between the effective phase mismatch δ and the Stokes (anti-Stokes) wavelengths, with $\lambda_{pump} = 1064$ nm, $P_0 = 2.2$ kW, and $d = 1.7$ μm . When $\delta = 0$, the wavelengths represent the Stokes (anti-Stokes) phase-matching condition. The black and blue lines correspond to Stokes and anti-Stokes, respectively. (For interpretation of the references to colour in this figure legend, the reader is referred to the web version of this article.)

the SBS can be enhanced [48–51]. In OFNs, the ability to strongly confine both optical and acoustic modes on the nanoscale has introduced new opportunities to control their interaction and attracted increasing attention since 2014.

The acoustic wave is driven by the electrostriction from the interference of the pump and scattered fields. The pump field is scattered by the acoustic wave. During the scattering event, the energy and the momentum are conserved. The relationships between the frequencies and wave vectors of these waves are as follows:

$$\begin{cases} \Omega_B = \omega_p - \omega_s \\ \vec{k}_b = \vec{k}_p - \vec{k}_s \end{cases}, \quad (18)$$

where $\Omega_B = \nu_b |\vec{k}_b|$ is the frequency of the acoustic wave, ω_p and ω_s are the frequencies of the pump and Stokes fields, respectively; \vec{k}_b is the wave vector of the acoustic wave; \vec{k}_p and \vec{k}_s are the wave vectors of the pump and Stokes fields, respectively, and ν_b is the velocity of the acoustic wave. Because the velocity of the acoustic wave is several orders of magnitude smaller than the velocity of light, we have

$$\Omega_B = \nu_b |\vec{k}_b| \approx 2\nu_b |\vec{k}_p| \sin(\psi/2), \quad (19)$$

where ψ is the angle between the pump and Stokes fields.

In particular, when $\psi = 0$ (in the forward direction), $\Omega_B \approx 0$ and $\omega_s \approx \omega_p$, and when $\psi = \pi$ (in the backward direction), Ω_B is maximized, and the Brillouin shift is

$$\nu_B = \Omega_B/2\pi = 2n\nu_A/\lambda_p. \quad (20)$$

Here, λ_p is the wavelength of the pump field.

Currently, SBS is usually attributed to not only bulk effects but also boundary effect [50,52]. The radiation pressure is greatly strengthened in optical OFNs owing to field confinement, which differs from the situation in conventional fibers. Two kinds of optical forces influence the SBS. Electrostrictive forces modulate the refractive index of the material, generating acoustic waves and thereby yielding bulk acoustic modes (shear and longitudinal waves). When the diameter of an OFN is on the subwavelength scale, the radiation pressure greatly impacts the boundary of the waveguide and induces vibration of the surface. The created sound wave is called a surface acoustic wave. Nevertheless, two effects (bulk effects and boundary effects) in SBS can completely counteract each other in the OFN [53]. These works provide an alternative mechanism to enhance or suppress SBS in OFNs. The control of the photon–phonon interaction is a step towards the practical application of the CMOS-compatible silicon chips, the hybrid photonic–phononic design [54], a new type of monolithic comb resonator [55,56], and other Brillouin devices.

To calculate the SBS shifts, one must obtain the acoustic mode, which creates a perturbation profile, both on the surface and throughout the wire cross section. The acoustic modes in a cylindrical-rod geometry can be categorized in symmetry-based modal

families and can be calculated analytically. The fundamental optical mode interacts most efficiently with two acoustic mode families: axially symmetric radial (R_{0m}) modes and axially asymmetric torsional-radial (TR_{2m}) modes. The fundamental modes in each family— R_{01} and TR_{21} —as shown in Fig. 15, are of particular interest because they have the largest acoustic displacement near the surface. In contrast to conventional SMF with a main peak at only ~ 11 GHz, there are many SBS frequencies because of the abundance of acoustic modes in OFNs.

Fig. 16 shows the typical Brillouin spectrum of an OFN measured using an optical heterodyne-detection method in a sample with a waist diameter of $0.7 \mu\text{m}$. The sample, which has a relatively short waist length of ~ 20 mm, is pumped with an input power of 1.5 W for a stronger signal. The spectrum has several peaks with different weights and linewidths in the range of 5 – 12 GHz. Except for the 10.844 -GHz peak originating from untapered SMF pigtaileds, all the peaks originate from the waist and transition regions of the sample.

There are few reports of experimental demonstrations of SBS in OFNs because of the weak SBS signal and the challenging fabrication of long and thin uniform OFNs. In 2014, Beugnot et al. demonstrated and reported the observation of surface acoustic wave Brillouin scattering in the backward direction for the first time, which means that boundary effects also influence SBS [57]. When the diameter of an OFN is on the subwavelength scale, radiation pressure greatly impacts the boundary of the waveguide and induces vibration of the surface. The created sound wave is called a surface acoustic wave. According to Ref. [57], the acoustic velocity significantly differs among surface, shear, and longitudinal waves. Surface waves travel at a velocity between 0.87 and 0.95 times that of a shear wave (for fused silica, the velocity is 3400 ms^{-1}). This gives rise to new optical sidebands down-shifted from 6 GHz in the light spectrum. Numerical simulations have been performed to validate the experimental measurements. A numerical simulation of the full acoustic-wave spectrum and displacements in silica OFN is presented. This work may thus represent a landmark to foster the investigation of such surface waves in many different photonic platforms, such as PCFs and integrated optical devices (for example, chalcogenide and silicon chips). Florez et al. experimentally demonstrated the perfect cancellation of Brillouin scattering by engineering a silica OFN with exactly opposing photoelastic (bulk) and moving-boundary (boundary) effects [58]. Perturbation theory was used to numerically calculate the photoelastic and moving-boundary coupling coefficient. The two fundamental acoustic modes were obtained— R_{01} and TR_{21} —because they had the largest acoustic displacement near the surface. At a high frequency, these modes are pure surface waves. Even below the Rayleigh limit, a large surface displacement is expected. In the experiment, R_{01} was observed for small and large diameters; however, it was not observed (within the experimental noise limit) in the region around $1.1 \mu\text{m}$. This is clear evidence that photoelastic and moving-boundary effects can be offset in certain situations [58]. The results show the potential of optical OFN for low-threshold lasers and amplifiers.

Beside the backward Brillouin scattering in OFNs discussed above, there are few reports on forward stimulated Brillouin scattering in OFNs which has been extensively proposed and demonstrated in nanostructured PCFs or waveguides [59–61]. Kang et al. fabricated a high-quality (<0.2 dB) insertion loss 40 cm-long fiber taper with few-micrometer-diameter waist to study optical excitation of transverse acoustic modes at frequencies of a few gigahertz [62]. We believe it is important and interesting to investigate forward Brillouin scattering effect in nanoscale OFNs although the measurement is relatively complicated because forward Brillouin scattering effect has both fruitful physical insight and great potential in expanding the OFN applications ranging from fiber laser mode-locking to opto-acoustic signal processing.

5. Stimulated Raman scattering

Raman scattering is inelastic scattering. When incident photons interact with molecules, photons are scattered from molecules or atoms, and most of the emitted photons have the same energy and frequency as the incident photons. This is elastic scattering, i.e., Rayleigh scattering. If a small part of the incident photons has a different energy and frequency from the incident photons, it is inelastic

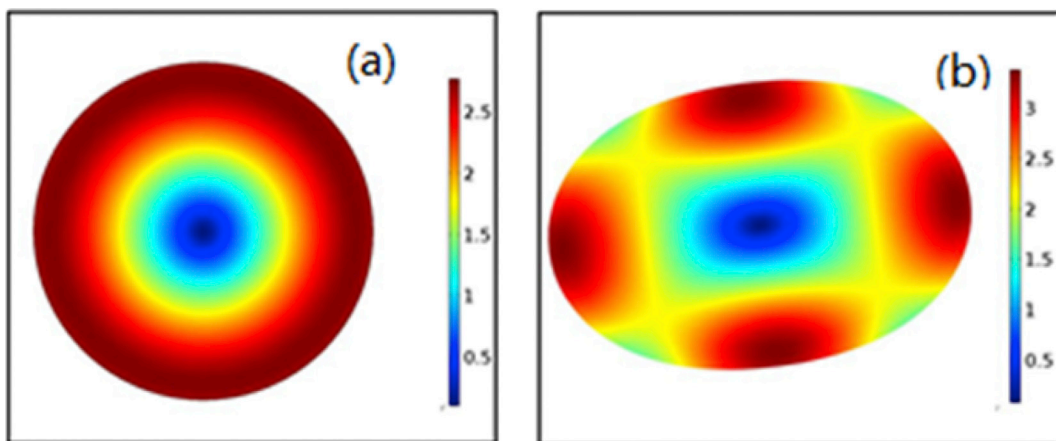


Fig. 15. Acoustic modes in an OFN. Two acoustic modes involved in SBS: the axially symmetric radial mode of the OFN shown in (a) and the axially asymmetric torsional-radial mode of the OFN shown in (b).

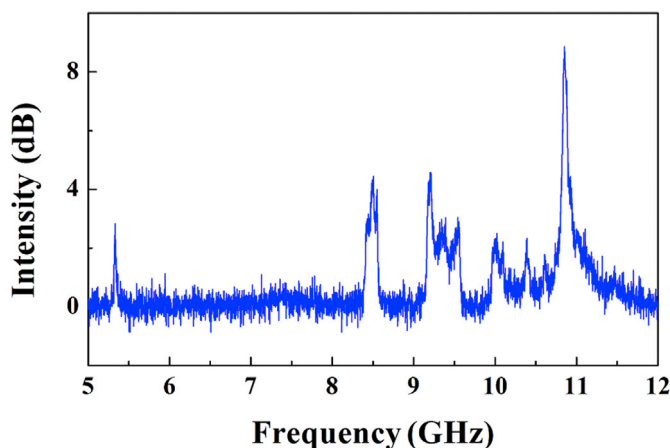


Fig. 16. Typical Brillouin backscattering spectra for a 700-nm OFN.

scattering, i.e., Raman scattering. Raman scattering includes Stokes scattering and anti-Stokes scattering and depends on the frequency shift. In fibers, Raman scattering is one of the important nonlinear processes with unique advantages and can be used to obtain broadband Raman amplifiers and tunable Raman lasers in undoped fibers.

The Raman gain determines the pump efficiency and is related to the cross section of spontaneous Raman scattering, which is related to the imaginary part of the third-order nonlinear susceptibility. In general, the gain depends on the composition of the fiber core and can vary significantly with the use of different dopants. The Raman-gain spectrum, as a function of the frequency difference between the pump and Stokes waves, extends over a large frequency range (up to 40 THz) with a broad peak located near 13 THz in silica fibers.

For OFNs, the large nonlinearity and high intensity due to the small cross section is beneficial to Raman scattering, giving rise to miniature Raman lasers and amplifiers. However, the Raman spectrum is still limited by the fiber materials.

A large evanescent field makes it possible to interact with external materials, induce different Raman spectra, and modify the Raman gain. It is reasonable to use an OFN to identify different gas and liquid molecules according to the characteristic spectrum. Thus far, few theoretical and experimental investigations have demonstrated the use of OFNs to detect liquids [63,64]. Moreover, Surface-enhanced Raman scattering (SERS) is a powerful technique to detect substances owing to its high sensitivity and fingerprint effect. Several fiber-optic SERS sensors have been reported [65–68].

6. Supercontinuum generation

GVD is a very important parameter in all fiber nonlinear applications, especially in SC generation [69], which has a very broad frequency spectrum and numerous applications in pulse compression, parametric amplifiers, SC-based WDM telecom sources, etc. [70–74]. SC was first observed in a fiber in 1976 when a pulse (10 ns) was pumped into a 20-m-long fiber [75]. Later, SC was observed in different kinds of fibers with diverse pump sources. SC generation typically occurs around the zero point of the GVD. The mechanisms responsible for SC generation are soliton fission, stimulated Raman scattering, FWM, SPM, and XPM. The nonlinear effects are induced by changes in the refractive index when intense pulses propagate through the nonlinear medium. To generate SC sources, very high optical power densities are needed for obtaining highly nonlinear optical effects. This can be realized by focusing the incident pulse on small-area tapered fibers. Additionally, tapered fibers are longer than bulk materials. To minimize the device length and maximize the broadening, it is necessary to optimize the dispersion profile of tapered fibers before pumping them. There are numerous reports on SC in tapered fibers with continuous-wave, nanosecond, picosecond, and femtosecond pulse pumps [71,74,76]. In 2000, femtosecond pulses were pumped into an OFN 2 μm in diameter, and SC was generated over two octaves (370–1545 nm at the 20-dB level) [77]. In 2012, when a 15-ps pulse was pumped into the fiber, it generated a 10-dB spectrum, from 780 to 1890 nm [78]. When the pump power is large enough, continuous-wave pulses can also generate SC. For example, a continuous-wave Raman fiber laser was used to pump an SMF 350 m in length, yielding SC (1434–1527 nm) [79]. Numerous applications based on SC have been investigated, such as spectral analysis, multi-wavelength optical sources, optical frequency metrology [80], and pulse compression [81].

7. Optomechanics

Optomechanics is a rapidly developing field undergoing significant and continuous progress. Various theoretical models for and experiments on optomechanical effects have been proposed and demonstrated in various configurations, in particular, in integrated photonic circuits based on nanoscale waveguides. However, because of the fiber size and device configuration, it is difficult to observe and utilize analogous optomechanical responses inside a conventional fiber system. Recent research into optomechanical effects in optical fibers mainly focused on one type of microstructured silica fiber [82]. Nevertheless, the fabrication and implementation of related devices and their corresponding applications present a significant challenge.

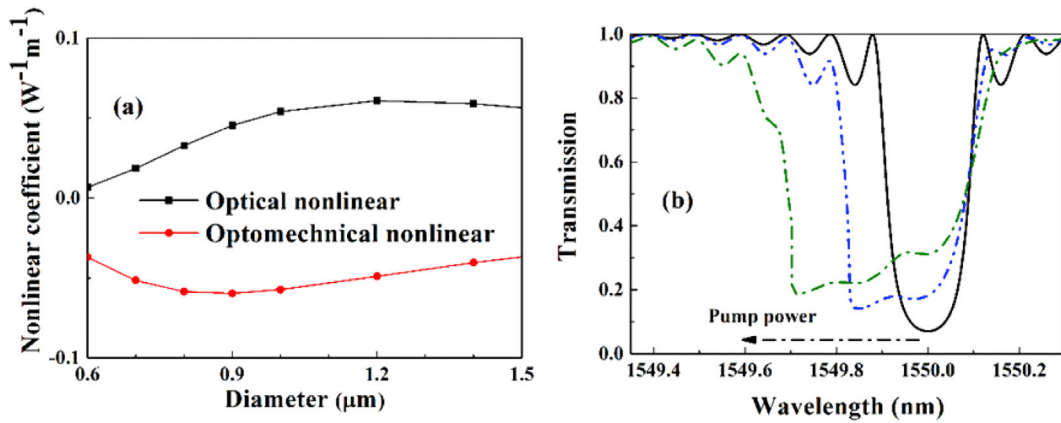


Fig. 17. (a) Values for the nonlinear and optomechanical parameters at different diameters. (b) Transmission spectra of the 600-nm-diameter OFN grating [88].

In consideration of their extreme lightness and free-standing status, OFNs have emerged as an ideal device to examine the influence of a weak optical force. Roughly, the mass of a 200-nm-diameter 10-μm-length microfiber is ~ 0.7 pg/ ~ 6.8 fN (in weight) which is the same level with the radiation pressure of light with a power of 1 μW. It means that the optical force is relatively large to handle the OFN.

In OFNs, typical optomechanical effects include the transversal optical gradient force and radiation pressure and the longitudinal radiation pressure. Sometimes, electrostrictive forces for Brillouin scattering can also be considered as a kind of optomechanical effect.

The transversal optical gradient force can be used to optically tune effective index in a slot OFN or coupling between two suspended OFNs; however, this has not been experimentally demonstrated. In most cases, the transversal optical gradient force outside an OFN was used to trap and deliver microparticles working together with longitudinal radiation pressure [83–85]. The transversal radiation pressure inside an OFN has only been theoretically investigated, revealing that it is possible to induce a photoelastic effect and influence the nonlinear index and Brillouin gain.

The longitudinal radiation pressure inside an OFN can only be found when the OFN is longitudinally non-uniform, such as the endface. Theoretical results show that the guided light exerts no net time-averaged longitudinal force on the uniform fiber but has a significant overall pulling force of 0.4 pN/mW acting on a 450-nm-diameter fiber tip at a wavelength of 980 nm due to the scattering of the end face [86]. In 2008, She et al. directly observed the sideways displacement of the fiber tip due to an optical push force on the endface and presented their opinion on the debate regarding Abraham's and Minkowski's momentum theory [87]. Longitudinal optical force can also be realized in OFN gratings with a modulated index. In 2015, Luo et al. present a detailed analytical and theoretical model of the optomechanical effect in a system of silica OFN Bragg gratings with air cladding. They presented a set of steady-state optomechanical coupled-mode equations by inducing a time-average optomechanical nonlinear coefficient analogous to the optical Kerr nonlinear coefficient.

The strains from radiation pressure introduce additional period and refractive-index changes to the Bragg condition for coupling between forward and backward waves within the gratings, which results in a tunable bandwidth of the Bragg reflection. The simulation shows that the magnitude of the strain induced by radiation pressure can be controlled by the input light. This allows us to achieve an optically reconfigurable chirp in the grating period and is promising for introducing a new platform for more all-optical controllable applications.

Fig. 17a compares the optical nonlinear and optomechanical coefficients. The nonlinear Kerr coefficient is 2.6×10^{-20} m²/W, the effective photoelastic coefficient is 0.21, the Young's modulus is 70 GPa, and the Bragg wavelength is set to 1550 nm. The optical nonlinear coefficient is opposite to the optomechanical coefficient because the Kerr effect and photoelastic effect have opposite impacts on the index change in the grating. They are both considerably larger than that in standard fiber gratings with a diameter of 125 μm. The absolute values of both parameters continue to increase as the diameter decreases until reaching their peaks, at which light can no longer be tightly confined in thinner OFNs [88].

By solving the steady-state optomechanical coupled-mode equations with a semi-implicit Runge–Kutta method and iteration, the spectra and group delay of the optomechanical OFN grating can be obtained. Fig. 17b shows the transmission spectra of an OFN grating with a 600-nm diameter at four different output powers. Here, the grating length is 1 cm, and the coupling coefficient is 2 cm^{-1} [88].

As the light power increases, the shape of the spectra eventually becomes asymmetric, the bandwidth increases, and the minimum transmittance increases. These are consequences of the Kerr effect and optomechanical effects (including photoelastic effect and chirp induced by radiation pressure). A chirp in the grating period introduces a shift of the Bragg wavelength, which is the main reason for the broadening of the bandwidth and the increase in the transmittance. The group delay can be tuned by changing the power, and all-optical switching can be achieved at a certain incident wavelength [88].

8. Conclusions

OFNs allow for a large degree of dispersion engineering and maximal effective nonlinearities. Combination with other advantages

such as large evanescent fields OFNs is ideally suited to investigate nonlinear optical interactions and develop new nonlinear devices. Numerous nonlinear effects in OFNs have been explained: the Kerr effect, SHG, THG, FWM, SBS, Raman, SC, and optomechanics. Compared with conventional SMFs, nonlinear effects can be enhanced in a small size. With the incorporation of new high-nonlinearity materials and the demonstration of novel effects, OFNs should continue to provide unique nonlinear optical functionality at even lower power levels. Although OFNs are still in their early development, their use for optical-fiber devices pave the way for a host of additional applications for communications, sensing, and lasers.

Acknowledgments

The authors acknowledge financial support from the National key R&D program of China (2017YFA0303700) and National Natural Science Foundation of China (61535005 and 61475069). The authors gratefully acknowledge Meng-tao Mao, Wei Luo and Yun-chao Shi help for preparing the manuscripts.

References

- [1] R.S. Wagner, W.C. Ellis, Vapor-liquid-solid mechanism of single crystal growth, *Appl. Phys. Lett.* 4 (5) (1964) 89–90.
- [2] E.I. Givargizov, Fundamental aspects of VLS growth, *J. Cryst. Growth* 31 (1975) 20–30.
- [3] F. Bilodeau, et al., Compact, low-loss, fused biconical taper couplers: overcoupled operation and antisymmetric supermode cutoff, *Opt. Lett.* 12 (8) (1987) 634–636.
- [4] J. Bures, R. Ghosh, Power density of the evanescent field in the vicinity of a tapered fiber, *J. Opt. Soc. Am. A* 16 (8) (1999) 1992–1996.
- [5] S.G. Leon-Saval, et al., Supercontinuum generation in submicron fibre waveguides, *Opt. Express* 12 (13) (2004) 2864–2869.
- [6] T. Birks, G. Kakarantzas, P. Russell, All-fibre devices based on tapered fibres, in: *Optical Fiber Communication Conference*, Optical Society of America, Los Angeles, California, 2004.
- [7] M. Sumetsky, Y. Dulashko, A. Hale, Fabrication and study of bent and coiled free silica nanowires: self-coupling microloop optical interferometer, *Opt. Express* 12 (15) (2004) 3521–3531.
- [8] G. Brambilla, V. Finazzi, D.J. Richardson, Ultra-low-loss optical fiber nanotapers, *Opt. Express* 12 (10) (2004) 2258–2263.
- [9] Y. Jung, et al., Polarization-maintaining optical microfiber, *Opt. Lett.* 35 (12) (2010) 2034–2036.
- [10] Y. Jung, et al., Highly birefringent silica microfiber, *Opt. Lett.* 35 (3) (2010) 378–380.
- [11] H. Xuan, J. Ju, W. Jin, Highly birefringent optical microfibers, *Opt. Express* 18 (4) (2010) 3828–3839.
- [12] K. Jun-long, X. Fei, Y.-q. Lu, Highly birefringent slot-microfiber, *Photonics Technol. Lett. IEEE* 23 (15) (2011) 1034–1036.
- [13] V.R. Almeida, et al., Guiding and confining light in void nanostructure, *Opt. Lett.* 29 (11) (2004) 1209–1211.
- [14] K. Okamoto, *Fundamentals of Optical Waveguides*, second ed., Elsevier, Amsterdam ; Boston, 2006 xvi, 561 pp.
- [15] L.M. Tong, J.Y. Lou, E. Mazur, Single-mode guiding properties of subwavelength-diameter silica and silicon wire waveguides, *Opt. Express* 12 (6) (2004) 1025–1035.
- [16] G.P. Agrawal, *Applications of Nonlinear Fiber Optics*, second ed., Academic Press, Burlington, 2008, p. 528.
- [17] R.W. Boyd, *Nonlinear Optics*, Academic Press, San Diego, CA, 1992.
- [18] V.S. Afshar, T.M. Monro, A full vectorial model for pulse propagation in emerging waveguides with subwavelength structures part I: Kerr nonlinearity, *Opt. Express* 17 (4) (2009) 2298–2318.
- [19] W. Guo, et al., Ultra-flattened and low dispersion in engineered microfibers with highly efficient nonlinearity reduction, *Opt. Express* 19 (16) (2011) 15229–15235.
- [20] V. Guillaume, et al., Theoretical study of microfiber resonator devices exploiting a phase shift, *J. Opt. A Pure Appl. Opt.* 10 (2) (2008) 025303.
- [21] G. Vienne, et al., Observation of a nonlinear microfiber resonator, *Opt. Lett.* 33 (13) (2008) 1500–1502.
- [22] A. Coillet, et al., Slow and fast nonlinearities in microfiber resonators, in: *Asia Optical Fiber Communication and Optoelectronic Exposition and Conference*, Optical Society of America, Shanghai, 2008.
- [23] F. Xu, et al., Dispersion study of optical nanowire microcoil resonators, *IEEE J. Sel. Top. Quantum Electron.* 17 (4) (2011) 1102–1106.
- [24] V. Grubsky, A. Savchenko, Glass micro-fibers for efficient third harmonic generation, *Opt. Express* 13 (18) (2005) 6798–6806.
- [25] D.L. Nicácio, et al., Third-harmonic generation in GeO₂-doped silica single-mode optical fibers, *Appl. Phys. Lett.* 62 (18) (1993) 2179–2181.
- [26] J.K. Ranka, R.S. Windeler, A.J. Stentz, Optical properties of high-delta air-silica microstructure optical fibers, *Opt. Lett.* 25 (11) (2000) 796–798.
- [27] U. Wiedemann, et al., Measurement of submicrometre diameters of tapered optical fibres using harmonic generation, *Opt. Express* 18 (8) (2010) 7693–7704.
- [28] V. Grubsky, J. Feinberg, Phase-matched third-harmonic UV generation using low-order modes in a glass micro-fiber, *Opt. Commun.* 274 (2) (2007) 447–450.
- [29] R. Ismaeel, et al., Nonlinear microfiber loop resonators for resonantly enhanced third harmonic generation, *Opt. Lett.* 37 (24) (2012) 5121–5123.
- [30] T. Lee, et al., Broadband third harmonic generation in tapered silica fibres, *Opt. Express* 20 (8) (2012) 8503–8511.
- [31] Y. Sasaki, Y. Ohmori, Phase-matched sum-frequency light generation in optical fibers, *Appl. Phys. Lett.* 39 (6) (1981) 466–468.
- [32] Y. Fujii, et al., Sum-frequency light generation in optical fibers, *Opt. Lett.* 5 (2) (1980) 48–50.
- [33] U. Österberg, W. Margulis, Dye laser pumped by Nd:YAG laser pulses frequency doubled in a glass optical fiber, *Opt. Lett.* 11 (8) (1986) 516–518.
- [34] D.Z. Anderson, V. Mizrahi, J.E. Sipe, Model for second-harmonic generation in glass optical fibers based on asymmetric photoelectron emission from defect sites, *Opt. Lett.* 16 (11) (1991) 796–798.
- [35] W. Luo, et al., Efficient surface second-harmonic generation in slot micro/nano-fibers, *Opt. Express* 21 (9) (2013) 11554–11561.
- [36] J. Lægsgaard, Theory of surface second-harmonic generation in silica nanowires, *J. Opt. Soc. Am. B* 27 (7) (2010) 1317–1324.
- [37] M.A. Gouveia, et al., Second harmonic generation and enhancement in microfibers and loop resonators, *Appl. Phys. Lett.* 102 (20) (2013) 201120.
- [38] C. Daengngam, et al., Fabrication and characterization of periodically patterned silica fiber structures for enhanced second-order nonlinearity, *Opt. Express* 23 (6) (2015) 8113–8127.
- [39] F.J. Rodriguez, F.X. Wang, M. Kauranen, Calibration of the second-order nonlinear optical susceptibility of surface and bulk of glass, *Opt. Express* 16 (12) (2008) 8704–8710.
- [40] R. Stolen, J. Bjorkholm, Parametric amplification and frequency conversion in optical fibers, *IEEE J. Quantum Electron.* 18 (7) (1982) 1062–1072.
- [41] S.H. Tang, et al., Simulation of optical microfiber strain sensors based on four-wave mixing, *IEEE Sensors J.* 16 (9) (2016) 3068–3074.
- [42] K.S. Abedin, et al., Highly nondegenerate femtosecond four-wave mixing in tapered microstructure fiber, *Appl. Phys. Lett.* 81 (8) (2002) 1384–1386.
- [43] D. Törke, J. Teipel, H. Giessen, Manipulation of supercontinuum generation by stimulated cascaded four-wave mixing in tapered fibers, *Appl. Phys. B* 92 (2) (2008) 159.
- [44] Y.H. Li, Y.Y. Zhao, L.J. Wang, Demonstration of almost octave-spanning cascaded four-wave mixing in optical microfibers, *Opt. Lett.* 37 (16) (2012) 3441–3443.
- [45] L. Cui, et al., Generation of correlated photon pairs in micro/nano-fibers, *Opt. Lett.* 38 (23) (2013) 5063–5066.
- [46] M.I.M. Abdul Khudus, et al., Phase matched parametric amplification via four-wave mixing in optical microfibers, *Opt. Lett.* 41 (4) (2016) 761–764.
- [47] Y. Wu, et al., Generation of cascaded four-wave-mixing with graphene-coated microfiber, *Photonics Res.* 3 (2) (2015) A64–A68.
- [48] H. Shin, et al., Tailorable stimulated Brillouin scattering in nanoscale silicon waveguides, *Nat. Commun.* (2013) 4.
- [49] P.T. Rakich, et al., Giant enhancement of stimulated Brillouin scattering in the subwavelength limit, *Phys. Rev. X* 2 (1) (2012) 011008.

- [50] R. Van Laer, et al., Interaction between light and highly confined hypersound in a silicon photonic nanowire, *Nat. Photonics* 9 (3) (2015) 199–203.
- [51] E.A. Kittlaus, H. Shin, P.T. Rakich, Large Brillouin amplification in silicon, *arXiv Prepr. arXiv:1510.08495* (2015).
- [52] J.-C. Beugnot, et al., Brillouin light scattering from surface acoustic waves in a subwavelength-diameter optical fibre, *Nat. Commun.* (2014) 5.
- [53] O. Florez, et al., Brillouin scattering self-cancellation, *arXiv Prepr. arXiv:1601.05248* (2016).
- [54] H. Shin, et al., Control of coherent information via on-chip photonic–phononic emitter–receivers, *Nat. Commun.* (2015) 6.
- [55] D. Braje, L. Hollberg, S. Diddams, Brillouin-enhanced hyperparametric generation of an optical frequency comb in a monolithic highly nonlinear fiber cavity pumped by a cw laser, *Phys. Rev. Lett.* 102 (19) (2009) 193902.
- [56] J. Li, H. Lee, K.J. Vahala, Microwave synthesizer using an on-chip Brillouin oscillator, *Nat. Commun.* (2013) 4.
- [57] J.-C. Beugnot, et al., Brillouin light scattering from surface acoustic waves in a subwavelength-diameter optical fibre, *Nat. Commun.* 5 (2014) 5242.
- [58] O. Florez, et al., Brillouin scattering self-cancellation, *Nat. Commun.* 7 (2016) 11759.
- [59] P. Dainese, et al., Raman-like light scattering from acoustic phonons in photonic crystal fiber, *Opt. Express* 14 (9) (2006) 4141–4150.
- [60] G.S. Wiederhecker, et al., Coherent control of ultrahigh-frequency acoustic resonances in photonic crystal fibers, *Phys. Rev. Lett.* 100 (20) (2008).
- [61] M.S. Kang, Butsch, A., P.S.J. Russell, Reconfigurable light-driven opto-acoustic isolators in photonic crystal fibre, *Nat. Phot.* 5 (9) (2011) 549–553.
- [62] M.S. Kang, et al., Optical excitation and characterization of gigahertz acoustic resonances in optical fiber tapers, *Appl. Phys. Lett.* 93 (13) (2008) 131110.
- [63] L. Shan, et al., Stimulated Raman scattering in the evanescent field of liquid immersed tapered nanofibers, *Appl. Phys. Lett.* 102 (20) (2013) 201110.
- [64] L. Shan, et al., Design of nanofibers for efficient stimulated Raman scattering in the evanescent field, *J. Eur. Opt. Soc. Rapid Pub.* 8 (2013) 13030.
- [65] A. Lucotti, G. Zerbi, Fiber-optic SERS sensor with optimized geometry, *Sensors Actuators B Chem.* 121 (2) (2007) 356–364.
- [66] J. Cao, et al., One-pot hydrothermal synthesis of silver nanoplates on optical fiber tip for surface-enhanced Raman scattering, *Appl. Phys. Lett.* 104 (20) (2014) 201906.
- [67] J. Zhang, et al., Tapered fiber probe modified by Ag nanoparticles for SERS detection, *Plasmonics* (2015) 1–9.
- [68] Z. Huang, et al., Tapered optical fiber probe assembled with plasmonic nanostructures for Surface-enhanced Raman Scattering application, *ACS Appl. Mater. Interfaces* 7 (31) (2015) 17247–17254.
- [69] J.M.a.T. Dudley, *Supercontinuum Generation in Optical Fibers. Applications of Nonlinear Fiber Optics*, second ed., Cambridge University Press, 2008, p. 418.
- [70] D.A. Akimov, et al., Two-octave spectral broadening of subnanosecond Cr²⁺: forsterite femtosecond laser pulses in tapered fibers, *Appl. Phys. B-Lasers Opt.* 74 (4–5) (2002) 307–311.
- [71] G. Brambilla, et al., Supercontinuum generation in tapered bismuth silicate fibres, *Electron. Lett.* 41 (14) (2005) 795–797.
- [72] P. Falk, M.H. Frosz, O. Bang, Supercontinuum generation in a photonic crystal fiber with two zero-dispersion wavelengths tapered to all wavelengths, *Opt. Express* 13 (19) (2005) 7535–7540.
- [73] K.B. Shi, F.G. Omenetto, Z.W. Liu, Supercontinuum generation in an imaging fiber taper, *Opt. Express* 14 (25) (2006) 12359–12364.
- [74] W.J. Wadsworth, et al., Supercontinuum generation in photonic crystal fibers and optical fiber tapers: a novel light source, *J. Opt. Soc. Am. B-Optical Phys.* 19 (9) (2002) 2148–2155.
- [75] C. Lin, R.H. Stolen, New nanosecond continuum for excited-state spectroscopy, *Appl. Phys. Lett.* 28 (4) (1976) 216–218.
- [76] Z.Y. Wang, et al., Spectral phase and intensity evolutions of supercontinuum generation in a biconical tapered fiber, *Opt. Rev.* 14 (2) (2007) 81–85.
- [77] T.A. Birks, W.J. Wadsworth, P.S.J. Russell, Supercontinuum generation in tapered fibers, *Opt. Lett.* 25 (19) (2000) 1415–1417.
- [78] M. Liao, et al., Flat and broadband supercontinuum generation by four-wave mixing in a highly nonlinear tapered microstructured fiber, *Opt. Express* 20 (26) (2012) B574–B580.
- [79] M. González-Herráez, et al., Supercontinuum generation using a continuous-wave Raman fiber laser, *Opt. Commun.* 226 (1–6) (2003) 323–328.
- [80] R. Holzwarth, et al., Optical frequency synthesizer for precision spectroscopy, *Phys. Rev. Lett.* 85 (11) (2000) 2264–2267.
- [81] G. Chang, T.B. Norris, H.G. Winful, Optimization of supercontinuum generation in photonic crystal fibers for pulse compression, *Opt. Lett.* 28 (7) (2003) 546–548.
- [82] A. Butsch, et al., Optomechanical nonlinearity in dual-nanoweb structure suspended inside capillary fiber, *Phys. Rev. Lett.* 109 (18) (2012) 183904.
- [83] H. Lei, et al., Bidirectional optical transportation and controllable positioning of nanoparticles using an optical nanofiber, *Nanoscale* 4 (21) (2012) 6707–6709.
- [84] B. Li, et al., An all fiber apparatus for microparticles selective manipulation based on a variable ratio coupler and a microfiber, *Opt. Fiber Technol.* 31 (2016) 126–129.
- [85] G. Brambilla, et al., Optical manipulation of microspheres along a subwavelength optical wire, *Opt. Lett.* 32 (20) (2007) 3041–3043.
- [86] H. Yu, et al., Longitudinal Lorentz force on a subwavelength-diameter optical fiber, *Phys. Rev. A* 83 (5) (2011) 053830.
- [87] W. She, J. Yu, R. Feng, Observation of a push force on the end face of a nanometer silica filament exerted by outgoing light, *Phys. Rev. Lett.* 101 (24) (2008) 243601.
- [88] W. Luo, F. Xu, Y.-Q. Lu, Reconfigurable optical-force-drive chirp and delay line in micro- or nanofiber Bragg grating, *Phys. Rev. A* 91 (5) (2015) 053831.